ORIGINAL RESEARCH ARTICLE

Residual Stress Control of TiC-Enhanced NiTi Shape Memory Alloys Fabricated by Laser Engineered Net Shaping

Fei Chen, Wen Guo, Jiao Li, Yang Liu, Chi Zhang, Jiaqi Lu, Zhifeng Huang, and Qiang Shen

NiTi alloy has unique shape memory effect and superelasticity, but low strength limits its application. TiC has been identified as a suitable reinforcing phase for NiTi shape memory alloys (SMAs) since it does not undergo interface reactions and has a minimal impact on the shape memory effect. In this study, NiTi SMAs with 5 wt.% TiC addition are prepared by Laser Engineered Net Shaping (LENS). The incorporation of TiC and the fast cooling rate of LENS process generate significant residual stress, thus, heat treatment at 600 and 800 °C are performed for residual stress control. After heat treatment, the stress-induced martensite caused by residual stress disappears, where residual stress of NiTi SMAs decreases by 50-60% when compared to the sample without heat treatment. The optimal yield strength of 531 MPa is 47.1% higher than that of pure NiTi SMAs (361 MPa). Besides, NiTi SMAs undergoes a one-step phase transformation from austenite to martensite, while a two-step transformation including austenite-R phase-martensite is observed after heat treatment.

1. Introduction

NiTi shape memory alloys (SMAs) exhibit remarkable properties such as shape memory effect and superelasticity, which can be activated by temperature and force-induced phase transition (Ref 1). Upon heating, NiTi can recover its original

Fei Chen, Chaozhou Branch of Chemistry and Chemical Engineering Guangdong Laboratory, Chaozhou 521000 Guangdong, China; State Key Lab of Advanced Technology for Materials Synthesis and Processing, Wuhan University of Technology, Wuhan 430070, China; International School of Materials Science and Engineering, Wuhan University of Technology, Wuhan 430070, China; and Hubei Longzhong Laboratory, Xiangyang 441000, China; **Wen Guo, Yang Liu, Chi Zhang, Jiaqi Lu,** and **Qiang Shen**, State Key Lab of Advanced Technology for Materials Synthesis and Processing, Wuhan University of Technology, Wuhan 430070, China; **Jiao Li**, The School of Arts, Hubei University of Education, Wuhan, China; **Zhifeng Huang**, State Key Lab of Advanced Technology for Materials Synthesis and Processing, Wuhan University of Technology, Wuhan 430070, China; and International School of Materials Science and Engineering, Wuhan University of Technology, Wuhan 430070, China. Contact e-mails: chenfei027@whut.edu.cn and lijiao@whhxit.edu.cn.

shape after deformation. Due to its excellent properties such as good corrosion resistance, biocompatibility, and superelastic stability, NiTi alloys are widely applied in various fields and large-scale industrial components such as aerospace, robotics, biomedical, weapons equipment, automotive industries, and elastocaloric cooling (Ref 2, 3, 4, 5, 6, 7, 8, and 9).

To explore the application of NiTi alloy at higher levels of strength, metal–matrix composites (MMCs) emerge as a highly effective solution. MMCs combine the ductility, toughness, and plasticity of metals with the rigidity, wear resistance, and corrosion resistance of ceramics. In the case of NiTi, it is necessary to combine the excellent properties of ceramics and metals while minimizing the impact on superelasticity and shape memory effect. The TiC ceramic phase exhibits stability within the NiTi matrix, not reacting with the NiTi matrix to form other intermediate phases (Ref 10, 11). Twinning in the NiTi alloy matrix can alleviate the thermal stress mismatch between the Ni-Ti matrix and TiC, thereby reducing the impact on the shape memory effect (Ref 12). However, during the additive manufacturing process, due to the high laser energy, there is a phenomenon of carbon diffusion. Zhang et al. (Ref 13) prepare and study the precipitation mechanism of the Ni_4Ti_3 phase in NiTi and 10 wt.% TiC-NiTi composite based on directed energy deposition (DED) and evaluated its mechanical properties through nanoindentation.

The preparation methods for NiTi and its composites are diverse, encompassing traditional powder metallurgy, laser additive manufacturing, as well as casting, forging, vacuum melting, and metal injection molding. Compared with traditional powder metallurgy, laser additive manufacturing has higher design freedom and can achieve near-net shape of complex structures (Ref 14), which shortens the processing cycle. In addition, during the laser additive manufacturing process, each position of the material undergoes rapid melting and solidification, is in a non-equilibrium solidifica-

tion state, and has a complex thermal history (Ref 15). This can result in microstructure and properties of the material that are different from those of traditional powder metallurgy. Residual stress is inherently induced within materials throughout the manufacturing process, significantly affecting the material properties. However, various mitigation strategies can be employed to manage and reduce residual stress (Ref 16). Researchers often reduce the internal residual stress of materials by optimizing process parameters, preheating, controlling cooling rates, and heat treatment. Edoardo Capello (Ref 17) suggested that residual stress can be controlled during the material turning process by adjusting parameters such as feed rate, tool nose radius, and to a minor extent, the entrance angle. E.M. Anawa et al (Ref 18) also pointed out that selecting appropriate laser power and welding speed can effectively reduce residual stress during the laser welding process. Preheating the substrate in welding or additive manufacturing can reduce the thermal gradient, thereby alleviating residual stress. Jung Eun Choi et al (Ref 19) have noted that a slow cooling rate can effectively eliminate residual stress during the ceramic sintering process.

Research on residual stress in additive manufacturing processes mainly focuses on the combination of numerical simulation and experimental process optimization (Ref 20). In terms of the latter, there is a particular emphasis on optimizing scanning strategies and controlling laser energy density (i.e., laser power, scanning speed, layer thickness), as well as implementing pre- and post-processing measures. By combining numerical simulation with experimental process optimization, researchers aim to reduce residual stress in additive manufacturing. J. Robinson et al. (Ref 21) compare and study eight different scanning strategies based on different residual stress testing methods and found that in the case of unidirectional scanning strategy, the residual stress in the material is twice as large in the parallel direction compared to the direction perpendicular to the building direction, while the XY alternating strategy provided the most uniform distribution and the lowest measured residual stress. Yang Zhang et al. (Ref 22) monitor the thermal history of four scanning strategies (unidirectional, bidirectional, bidirectional 90-degree rotation, and inward spiral) using infrared thermal imaging, and compare the microstructure, mechanical properties, and residual stress of the samples under the four strategies. The residual stress in material under the inward spiral pattern is larger, resulting in internal crack defects and poor mechanical properties. The research by Thomas Simson and L. Mugwagwa (Ref 23, 24) shows that the residual stress in the material increase with the increase in laser energy density. In terms of pre-printing processing, researchers generally (Ref 25, 26) show that preheating the substrate can effectively reduce the residual stress in the material during printing. In post-printing processing, heat treatment is commonly used to reduce residual stress (Ref 27, 28).

In this study, a significant improvement in yield strength of NiTi is achieved by incorporating TiC. The yield strength is increased from 361 MPa to 531 MPa. A heat treatment process is employed to control the internal residual stress, which effectively eliminate stress-induced martensitic transformation that can arise from high residual stress.

Table 1 Chemical composition (wt.%) of NiTi and TiC

Material	%Ti	%Ni	%C	%O + N
NiTi	Bal	56.46	0.003	0.037
TiC	Bal	…	19.4	< 0.06

2. Experimental Procedures

2.1 Raw Materials

The raw materials utilize in this study comprise gas-atomized NiTi spherical powder, obtained from Avimetal Powder Metallurgy Technology Co, Ltd, with particle sizes ranging from 53 to 150 μm, and irregular TiC powder, sourced from Beijing Zhongke Yannuo New Material Technology Co, Ltd, with particle sizes ranging from 50 to 150 μm. The chemical composition of NiTi and TiC, presented as weight percentages, can be found in Table 1. The powder mixtures are prepared using a mass ratio of 5 wt.% TiC to NiTi. For the pretreatment of the mixed powders, a planetary ball milling machine is employed, with corundum balls serving as the milling balls. The weight ratio of the milling balls to the powders was set at 0.8:1. Both the milling bowls and the sun wheel rotated at a speed of 200 rpm. The processing time was set to 4 hours. The sphericity of the powder after mixing is evaluated to be suitable for application in the LENS system, as depicted in Fig. 1.

2.2 Materials Preparation

Figure 2 illustrates the manufacturing process, which is conducted using the LENS 150 system equipped with a 400-W fiber laser. In order to prevent oxidation and enhance deposition, the system chamber is purged with argon gas to maintain oxygen levels below 100 ppm. Argon gas is employed to deliver the NiTi and TiC powder into the molten pool. The scanning direction between two consecutive layers, N and N + 1, is rotated by 90 degrees. For a comprehensive overview of the designed process parameters, please refer to Table 2.

After LENS processing, the NiTi-5% TiC specimens is heat treated at 600 and 800 °C for 2 h at the heat rates of 10 K/min and then furnace cooling to room temperature.

2.3 Characterization of Microstructure and Properties

To investigate the microstructure and phase characteristics of the samples, specimens are prepared in their as-built conditions using the standard metallography procedure. Following this, the specimens undergo polishing according to the general metallography procedure. Subsequently, the polished specimens are subjected to etching using an acidic solution containing 1 ml HF, 4 ml HNO$_3$, and 5 ml H$_2$O. Microstructural analysis and chemical composition analysis are conducted using a scanning electron microscope (SEM). X-ray diffraction (XRD) analysis is performed with a step size of 2° per minute in the range of 30 to 90°. Electron backscatter diffraction (EBSD) analysis is carried out using an EDAX-TSL system under the following conditions: acceleration voltage of 20 kV, tilt angle of 70°, and a step size of 150 nm. In order to
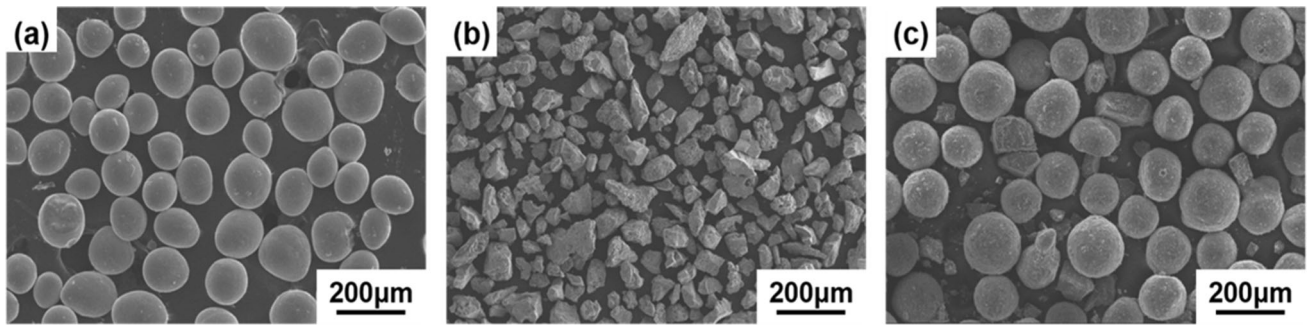
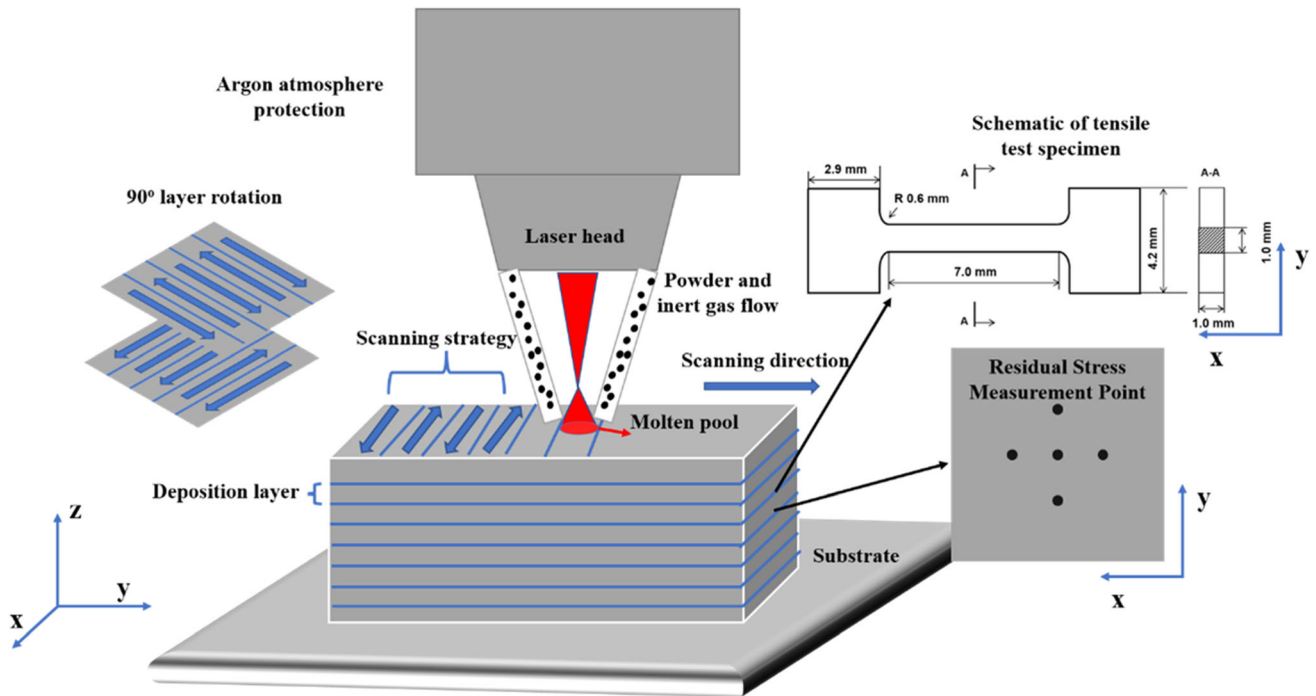**Fig. 1** (a) SEM image of NiTi powder; (b) SEM image of TiC powder; (c) SEM image of NiTi and TiC mix powder

Fig. 2 LENS system and scanning strategy

Table 2 Processing parameters of the NiTi and NiTi-5% TiC

Laser power, W	Scanning speed, mm/min	Laser spot size, mm	Layer thickness, mm	TiC mass ratios, wt%
330	50	2	0.2	0
330	50	2	0.2	5

determine the phase transformation temperatures of the NiTi samples with 5 wt.% TiC, a differential scanning calorimetry (DSC) test is performed with heating and cooling rates of 10 K/min, within a temperature range of − 80 to 150 °C.

Tensile tests are conducted at room temperature using a universal material testing machine (Instron 5982) with a testing rate of 0.42 mm/min. Each case is tested with a minimum of three samples to ensure accuracy and reliability. The mechan-ical properties, including yield strength, ultimate strength, and elongation to fracture, are measured and recorded.

Residual stress in the specimens is measured using an x-ray diffractometer equipped with Co-Kα radiation, and calculated using the x-ray diffraction sin 2ψ method.

3. Results and Discussion

3.1 Effect of TiC Addition on Microstructure and Mechanical Properties of NiTi SMAs

Figure 3(a) and (b) presents the optical microscopy images of NiTi and NiTi-5% TiC at a laser power of 330W. There are no obvious cracks and pore defects inside the sample. The density of the samples, measured using the Archimedes drainage method, is 99.63 and 99.46% respectively, indicating superior printability.

Figue 4(a) illustrates the x-ray diffraction (XRD) patterns of the raw powder, NiTi and NiTi-5% TiC. The raw powder and the samples processed by LENS are composed of austenite
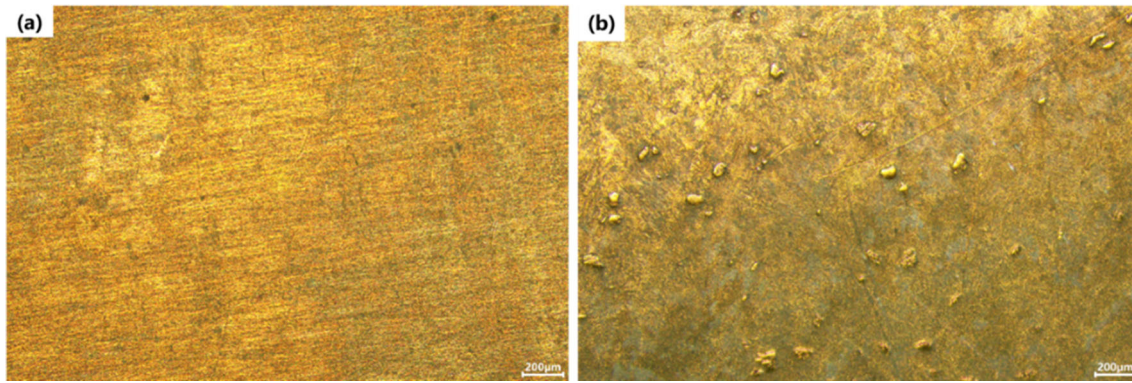
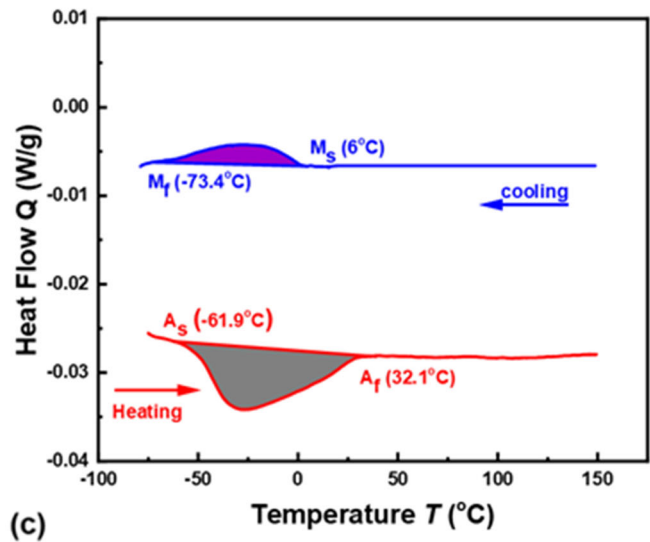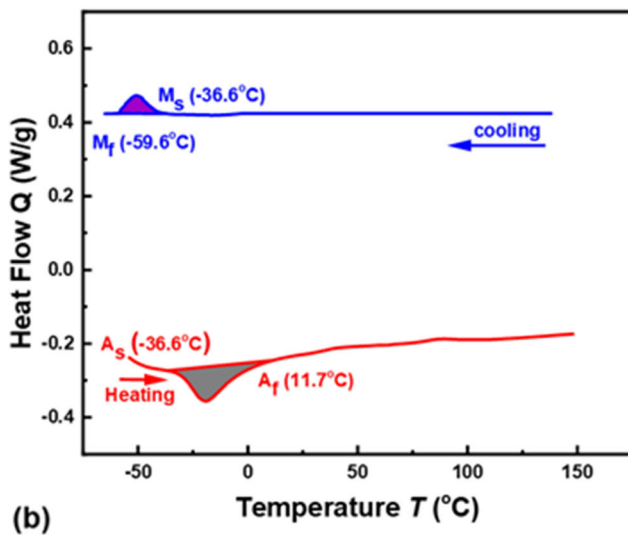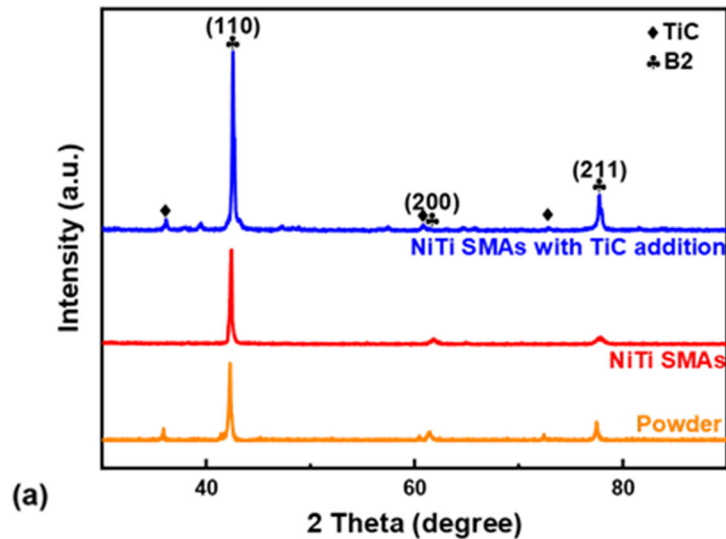**Fig. 3** OM images: (a) NiTi; (b) NiTi-5% TiC

Fig. 4 (a) XRD images of raw powder, NiTi and NiTi-5% TiC; DSC curves: (b) NiTi, (c) NiTi-5% TiC

phase (B2). Figure 4(b) depicts the DSC curves of NiTi. The Martensite start temperature (M_s), Martensite finish temperature (M_f), Austenite start temperature (A_s), Austenite finish temperature (A_f), are -36.6, -59.6, -36.6 and 11.7 °C, respectively. Figure 4(c) depicts the DSC curves of NiTi-5% TiC. The M_s, M_f, A_s, A_f, are 6, -74.3, -61.9, 32.1 °C, respectively.

In the comparative analysis of the DSC curves between pure NiTi and NiTi incorporated with 5 wt.% TiC, a discernible broadening in the phase transition range was observed. During the cooling stage, the phase transition range of the NiTi-5wt.% TiC composite is extended from an initial range of -36.6 to -59.6 °C to a more comprehensive range of -6 to
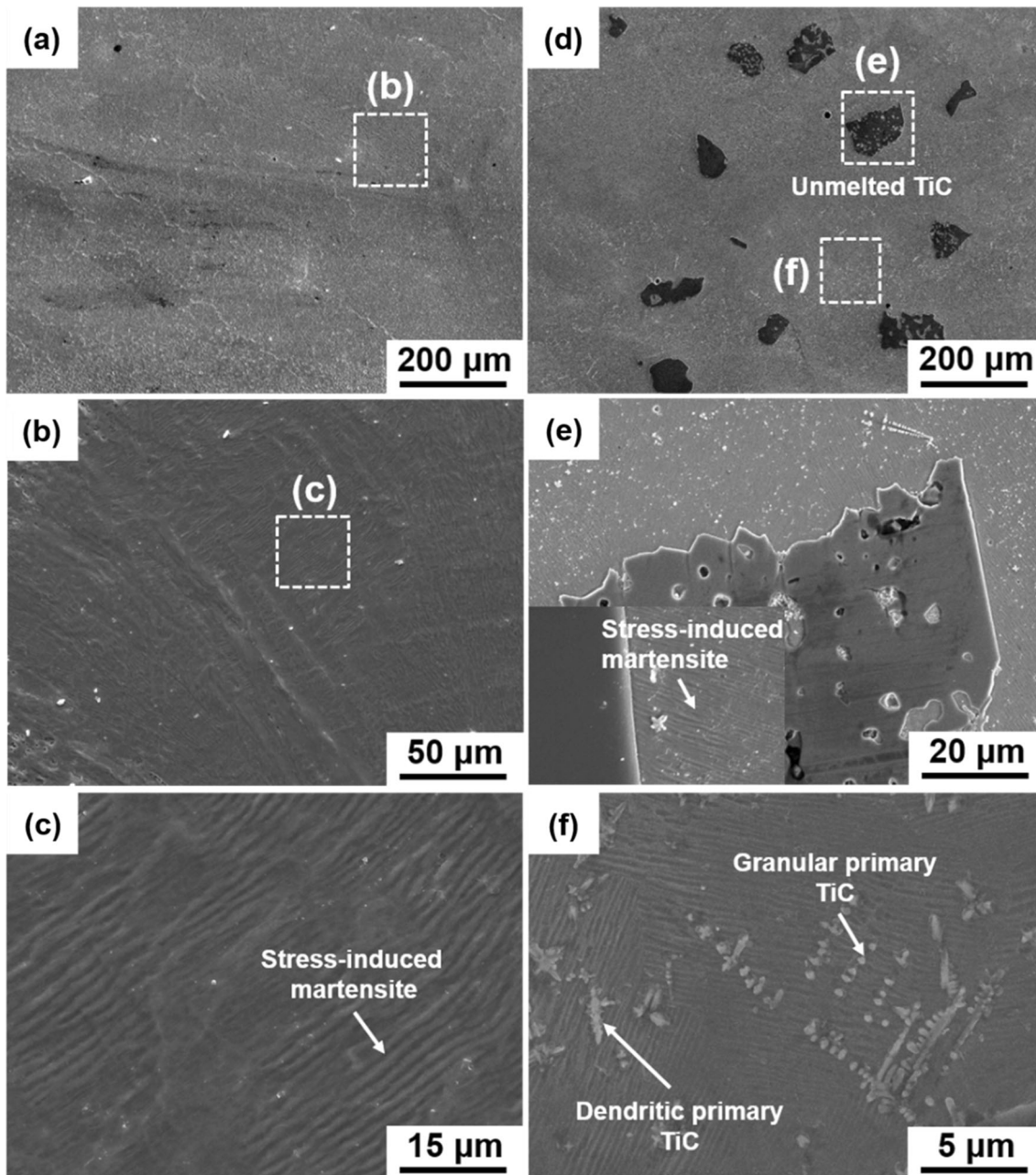
Fig. 5 SEM images: (a)-(c) NiTi; (d)-(f) NiTi-5% TiC

74.3 °C. Analogously, in the heating stage, the modified material exhibits an expanded phase transition range, stretching from − 61.9 to 32.1 °C, as opposed to the − 36.6 to 11.7 °C range observed in pure NiTi. Quantitatively, this represents a substantial expansion in the phase transition temperature ranges by approximately 249.1 and 94.6% for the cooling and heating stages, respectively. This observed phenomenon can be attributed to the formation of TiC dendrites within the NiTi matrix, which plays a pivotal role in influencing the local Ni/Ti ratio, and consequently, affecting the local phase transition temperature. As the dendritic TiC initiates formation and undergoes growth, it predominantly consumes Ti elements, thereby modifying the local Ni/Ti ratio in its immediate vicinity. Contrarily, the Ni/Ti ratio in the overarching NiTi matrix predominantly remains unaltered or constant. This

induced disparity in the Ni/Ti ratios across different regions within the material leads to the manifestation of a more diversified and broader range of phase transformation temperatures. (Ref 29).

Figure 5(a), (b) and (c) illustrates the microstructure of NiTi with 330 W laser power. The sample is dense, without obvious cracks, pores, and other defects. The matrix predominantly consists of the B2 phase, accompanied by twinned martensite structures, which are attributed to the influence of residual stress. Figure 5(d), (e) and (f) illustrates the microstructure of NiTi-5% TiC, consisting of the B2 matrix, twinned martensite, and three distinct types of TiC with different morphologies: granular primary TiC (GPT), dendritic primary TiC (DPT), and unmelted TiC (UMT) (Ref 30, 31).
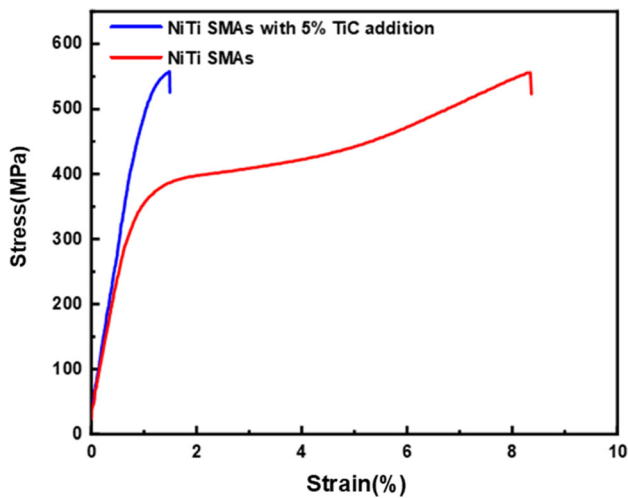
Fig. 6 Strain-stress curves of NiTi and NiTi-5% TiC

The NiTi matrix displays a typical detwinned microstructure induced by residual stress, which caused by the thermal gradient attributed to the faster cooling rate during the additive manufacturing process, the shrinkage and solidification of the material (Ref 32) and the mismatch of the thermal expansion coefficient between TiC and the NiTi matrix during additive manufacturing (Ref 33, 34). As the temperature in the melt pool rises to a certain degree, the edge of TiC particles will melt, allowing more carbon atoms to dissolve into the melt pool. An in-situ reaction between Ti and C in the melt pool leads to the formation of primary TiC. With the laser scanning next layer, the temperature of the melt pool increases, further promoting the melting of TiC particles. At the same time, the C concentration in the melt pool increases, and the diffusion rate of Ti and C elements increases. Due to the high cooling rate during the additive manufacturing process, the combination of Ti and C elements precipitates in a typical dendritic structure (Ref 35, 36).

Figure 6 shows the tensile properties of NiTi and NiTi-5% TiC. The yield strength of NiTi is 361 MPa with an elongation of 8.36%. Upon the addition of 5wt.% TiC, the yield strength of NiTi SMAs increases by 47.1% to 531 MPa, while the elongation decreases significantly to 1.5%.

Figure 7(a) and (b) shows the fracture morphology of NiTi. There are numerous dimples on the fracture surface, indicating that the material undergoes ductile fracture. Figure 7(c) and (d) presents the fracture morphology of NiTi-5% TiC. The tear-edges and cleavage steps suggest that after adding 5 wt.% NiTi mainly failed in a brittle manner. In addition, cracks are observed in the unmelted TiC, indicating that cracks are preferentially formed in the unmelted TiC during the tensile process and then propagated to the material failure along the bonding interface (Ref 37, 38). Micro-pores and micro-cracks are also observed in the magnified fracture morphology. Notably, Figure 7(d) shows an indentation left by the broken dendritic TiC in the NiTi matrix, implying that dendritic TiC is a brittle phase (Ref 36, 37) that is prone to breakage during the tensile process, leaving micro-cracks in the matrix.

During the tensile process, the brittle UMT and DPT distributes in the matrix hinder the plastic deformation of the matrix and cause stress concentration around these brittle phases (Ref 39, 40). The protruding edges of the UMT and the dendritic tips can easily become stress concentration points and crack to release stress during the tensile process. The cracking of these brittle phases leads to a decrease in the elongation. The TiC particles in the melt pool often have a pinching effect on the movement of grains and phase boundaries. The addition of TiC can refine the grain size and play a role in grain refinement. Moreover, the dissolved C causes solid solution strengthening of the matrix, and the precipitation strengthening of small-sized GPT is also beneficial for the strengthening of NiTi (Ref 30, 38, 40).

3.2 Effect of Heat Treatment on Microstructure of NiTi-5% TiC SMAs

Figure 8(a) displays the XRD curves of NiTi under 330 W laser power after heat treatment at 600 and 800 °C. The results reveal the appearance of Ni_4Ti_3 and B19' phases in NiTi after heat treatment. The peak intensity of TiC increases, and the peak intensity of Ni_4Ti_3 precipitated phase increases, while the content of the martensite phase in the matrix at room temperature increases with the increase in heat treatment temperature. Meanwhile, the Ni_3Ti phase also emerges. Figure 8(b) and (c) demonstrates the DSC curves of NiTi SMAs under 600 and 800 °C heat treatment conditions, respectively, at 330 W laser power. Compared with the as-built NiTi SMAs, the phase transition temperature increases, and the cooling curve shows a clear inflection point, indicating a two-step phase transformation from B2 phase to R phase and then to B19' phase. Also, with the increasing heat treatment temperature, the DSC curve peak become sharper.

Figure 9 illustrates the microstructure of NiTi-5% TiC under different heat treatment conditions. Figure 9(a) and (b) are the samples heat-treated at 600 °C for 2 hours. The NiTi matrix still contains a large amount of stress-induced martensitic phase, indicating that a significant residual stress exists inside. Meanwhile, a small amount of Ni_4Ti_3 phase precipitates inside the NiTi matrix. Figure 9(c) and (d) are the samples heat-treated at 800 °C for 2 hours. The stress-induced martensitic phase inside the matrix disappears, and the amount and size of Ni_4Ti_3 phase precipitated inside the matrix increase compared to the samples heat-treated at 600 °C. The Ni_4Ti_3 phase is randomly distributed and has no orientation.

As the temperature increases, the solubility of nickel in the matrix also increases. This higher solubility facilitates the formation of nickel-rich precipitates. These newly formed precipitates consume the available nickel content in the matrix, consequently resulting in an increase in the transformation temperature. (Ref 41). Heat treatment induces the precipitation of Ni_4Ti_3 phase in NiTi-5% TiC, and the presence of the Ni_4Ti_3 precipitate is accompanied by the generation of a strain field and a concentration gradient of Ni atoms around the Ni_4Ti_3 precipitate. This structure exhibits strong variant selection effects and strongly limits the growth of the martensite domain (Ref 42, 43, 44). Since the strain energy for R-phase formation is lower than that for monoclinic phase formation, the DSC curve shows a two-stage phase transition. Moreover, due to the TiC dendrites in the matrix, the local Ti/Ni ratio is different, resulting in an increased phase transition range in the DSC curve. Therefore, instead of two distinct phase transition peaks, there is a clear inflection point in the DSC curve. With increasing heat treatment temperature, the metastable Ni_4Ti_3 phase transforms into the stable Ni_3Ti phase (Ref 45), leading to the appearance of a Ni_3Ti peak in the XRD curve.
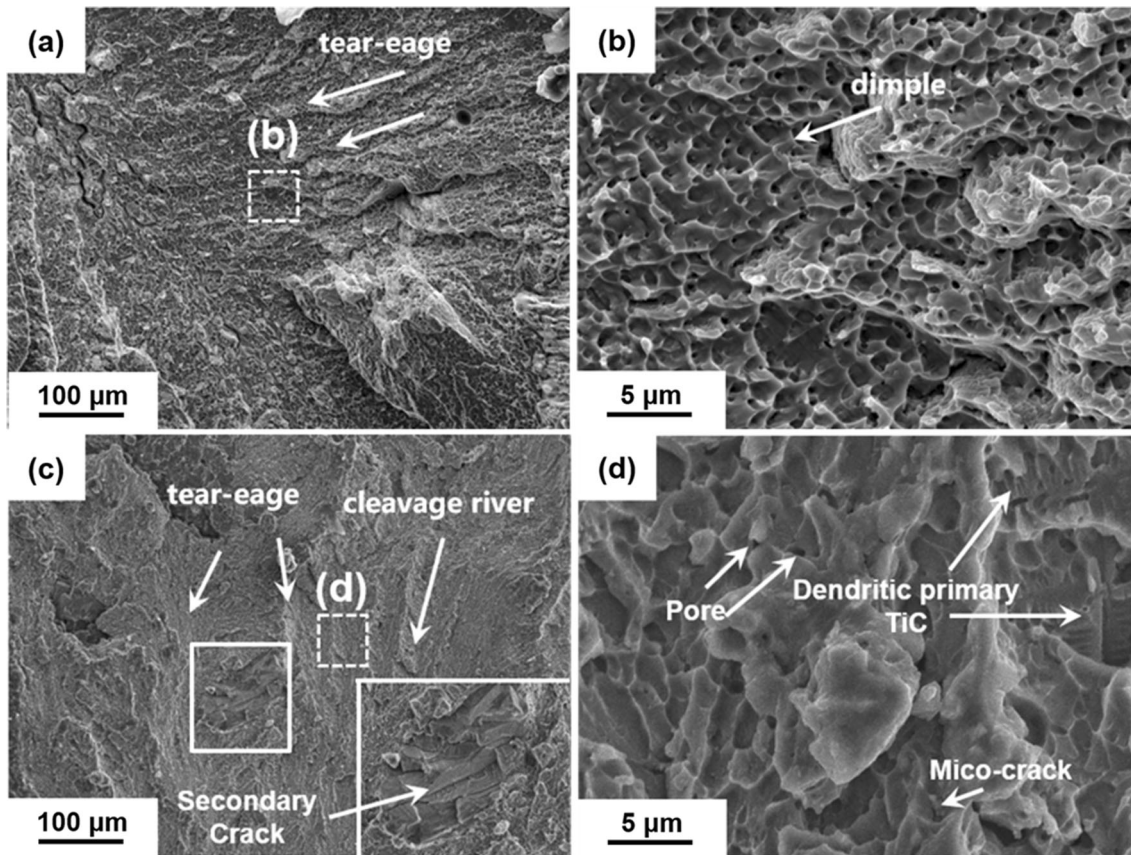
Fig. 7 The fracture morphology (a-b) NiTi; (c)-(d) NiTi-5% TiC

Additionally, the homogenization of C during the heat treatment process enhances the intensity of the TiC peak.

Figure 10(a), (b) and (c) displays the inverse pole figure (IPF maps of NiTi-5% TiC, and after 600 and 800 °C heat treatments. The LENS-produced NiTi-5% TiC exhibits columnar grains that grow along the direction of the melt pool. After heat treatment, some of the columnar grains transform into equiaxed grains, and the grain size increases. Figure 10(d), (e) and (f) shows the kernel average misorientation (KAM) maps of the NiTi-5% TiC, and after heat treatments at 600 and 800 °C. The LENS-produced NiTi-5% TiC exhibits a high density of dislocations, which decreases after 600 °C heat treatment and further decreases after 800 °C heat treatment. Figure 10(g), (h) and (i) displays the grain boundary maps of the NiTi-5% TiC, and after heat treatments at 600 and 800 °C. The LENS-produced NiTi SMAs has mainly small angle grain boundaries, which decrease after 600 and 800 °C heat treatments, while large angle grain boundaries increase. Figure 10(j), (k) and (l) illustrates the dislocation density of the material. For NiTi-5%TiC and under heat treatment conditions of 600 and 800 °C, the dislocation densities are $3.14644 \times 10^{13}/m^2$, $2.07544 \times 10^{12}/m^2$, and $13.1188 \times 10^{12}/m^2$, respectively. Heat treatments at 600 and 800 °C reduced the dislocation density by 34.03 and 58.31%, respectively.

The unique thermal history and melt pool behavior of additive manufacturing often result in columnar grains with epitaxial growth (Ref 46). High cooling rates during rapid solidification and repeated remelting processes lead to a thermodynamically non-equilibrium state, and the residual stress generated by contraction results in high dislocation density and low angle grain boundaries (Ref 47). Heat treatment can induce grain growth, grain boundary migration, and partial grain recrystallization. The density of low angle grain boundaries decreases as a result of these behaviors, during which the grain size increases, some columnar grains transform into equiaxed grains, and the residual stress is gradually released. Larger grains provide more space for dislocation movement and interaction, thereby reducing NiTi-5% TiC's dislocation density (Ref 48).

3.3 Residual Stress of NiTi-5% TiC SMAs

As additive manufacturing materials exhibit a strong preferred orientation, the (110) crystal plane peak with higher peak intensity is chosen for residual stress measurement. The non-distorted diffraction angle $2\theta_0$ for this peak is found to be 42.479°.

The relationship between residual stress (σ) and strain (ε) on the surface of the sample under plane stress is determined using the following elasticity theory equation (Ref 49, 50):

$$\frac{\partial(\varepsilon)}{\partial(\sin^2\Psi)} = \frac{(1+v)\sigma}{E}$$

The Bragg equation, $\lambda = 2d\sin\theta$, relates the wavelength of the incident x-ray (λ), the interplanar spacing of the crystal lattice (d), and the diffraction angle (θ), and gives the following relationship (Ref 49, 50):
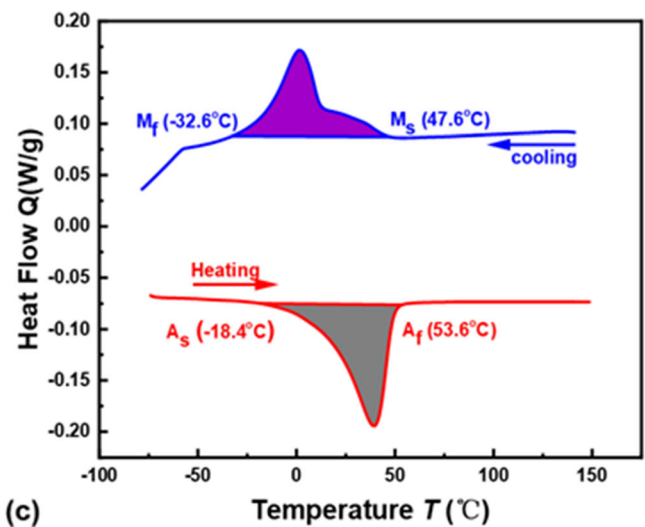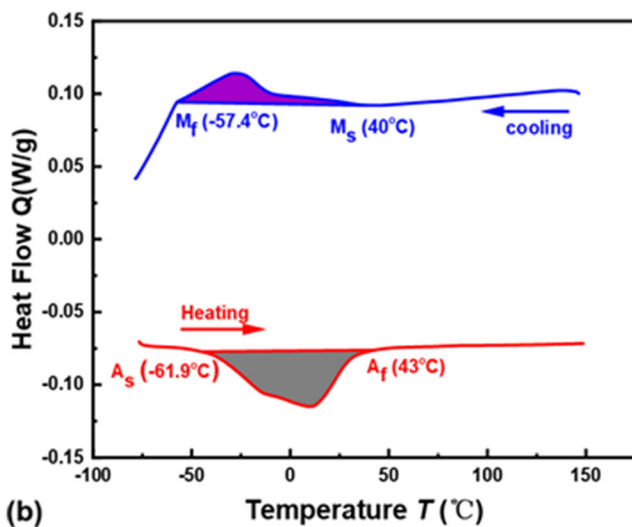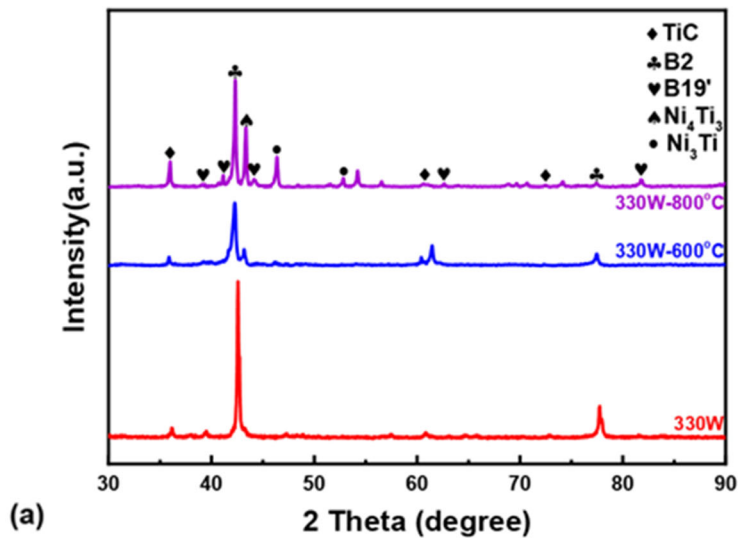
$$\frac{\Delta d}{d} = -\cot\theta\Delta\theta$$

Fig. 8 (a) XRD images of the NiTi-5% TiC with heat treatment. DSC cures of NiTi-5% TiC (b) heat treatment by 600 °C-2 h; (c) heat treatment by 800 °C-2 h

The strain (ε), is therefore expressed as:

$$\varepsilon = \frac{\Delta d}{d} = -\cot\theta_0(\theta - \theta_0)$$

The residual stress equation can be calculated using the 2θ angle measured directly by the diffractometer, which can be converted and used directly. The formula used for calculation is (Ref 43, 44, 45):

$$\sigma = -\left[\frac{E}{2(1+v)}\right]\cot\theta_0\left(\frac{\pi}{180}\right)\cdot\left\{\frac{\Delta(2\theta)}{\Delta(\sin^2\Psi)}\right\} = K\cdot M$$

where, K is the stress constant, M is the slope of 2θ and $\sin^2\Psi$, E is the Young's modulus, v is the Poisson's ratio, θ_0 is the diffraction angle under the undistorted condition (represented in radians by multiplying by $\pi/180$) , and ψ is the inclination angle between the diffracted plane and the plane normal of the sample. The peak position (2θ) corresponding to the maximum intensity is determined by counting data with $\sin^2\Psi$ values of

(0, 0.1, 0.2, 0.3, 0.4, 0.5). The slope M is determined by the linear equation least squares method.

The relationship between 2θ and $\sin^2\Psi$ is shown in Figure 10. The value of v is 0.33, and the value of E is obtained from the universal testing machine data. The numerical values of residual stress are shown in Table 3.

Figure 11 and Table 3 display the residual stress of NiTi-5% TiC at the center position, and the fitted line has a negative slope, indicating the existence of compressive stress. The residual stress of the as-built material is 359 MPa, and after heat treatment at 600 and 800 °C, the residual stress decrease to 251 and 58 MPa, respectively.

For the additive manufacturing process, the laser rapidly heats up the raw material powder, causing thermal expansion and generating thermal stress. Due to the rapid solidification behavior and the repeated remelting of the material during the stacking process, residual thermal stress accumulates within the solidified layer. As shown in Figure 10, under the 600 and 800 °C heat treatment conditions, the NiTi-5% TiC grains grow and re-arrange, dislocations slide and climb at high tempera-
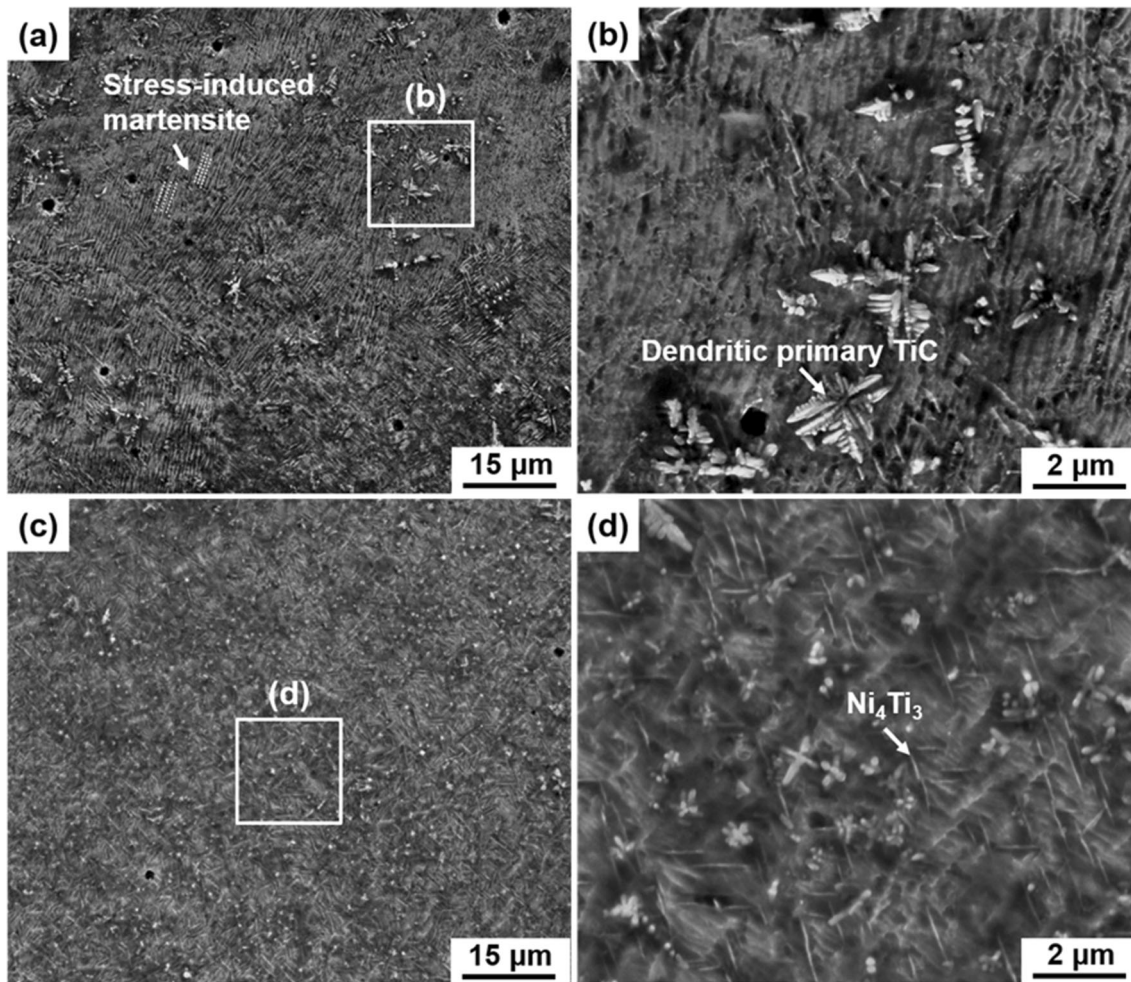
Fig. 9 SEM images for NiTi-5% TiC :(a)-(b) heat treatment by 600 °C-2 h; (c)-(d) heat treatment by 800 °C-2 h

tures, and low-angle grain boundaries are eliminated as the grains grow and recrystallize. The dislocation density decreases continuously with the increase in temperature, and NiTi-5% TiC residual stress is released.

3.4 Effect of Heat Treatment on Mechanical Properties of NiTi-5% TiC

Figure 12(a) displays the mechanical properties of NiTi-5% TiC under 600 and 800 °C heat treatment conditions with a laser power of 330 W. The yield strength of samples treated at 600 and 800 °C is 435 MPa and 225 MPa, respectively, and the elongation is 2.23 and 3.53%, respectively. Figure 12(b) demonstrates the recoverability of the material under a 2% pre-strain. The material exhibits superelasticity when treated at 600 °C, with a recoverability rate of 98%. Under the heat treatment condition of 800 °C, the material displays the shape memory effect. With a pre-strain of 2%, the strain recovery of the material after unloading is 1.26%. After heating the sample, the strain further recovers by 0.64%, leading to an overall recoverability rate of 95%. Figure 12(c) and (d) shows the cyclic stability of the material under different heat treatment conditions at 2% pre-strain and 20 cycles of cyclic tensile loading. As the number of cycles increases, the irreversible strain gradually accumulates, while the stress hysteresis decreases.

At laser power of 330 W, NiTi-5% TiC exhibits a high density of dislocations and large residual stress, which hinder the plastic deformation, resulting in higher yield strength and lower elongation (Ref 52). After heat treatment at 600 °C, the residual stress in NiTi-5% TiC is released, and its dislocation density decreases with the evolution of grains. At this temperature, the yield strength of NiTi-5% TiC decreases, and its elongation improves. After heat treatment at 800 °C, the residual stress and dislocation density within are further reduced. Additionally, the precipitation of Ni_4Ti_3 phase raises the transformation temperature of NiTi-5% TiC, resulting in the presence of martensite phase at room temperature, and thus significantly reducing its yield strength. The accumulation of irreversible strain in NiTi-5% TiC during cyclic loading can also be attributed to microstructural defects and the stabilization of stress-induced martensite. Due to the introduction of dislocations during the mechanical cycling process, the continuous accumulation of stress-induced martensite occurs, preventing a return to austenite upon unloading (Ref 52, 54, 55). TiC particles contribute to frictional resistance at the interface (Ref 12) and the lattice mismatch between the large-sized Ni_4Ti_3 phase and the B2 matrix phase results in stress hysteresis (Ref 42).
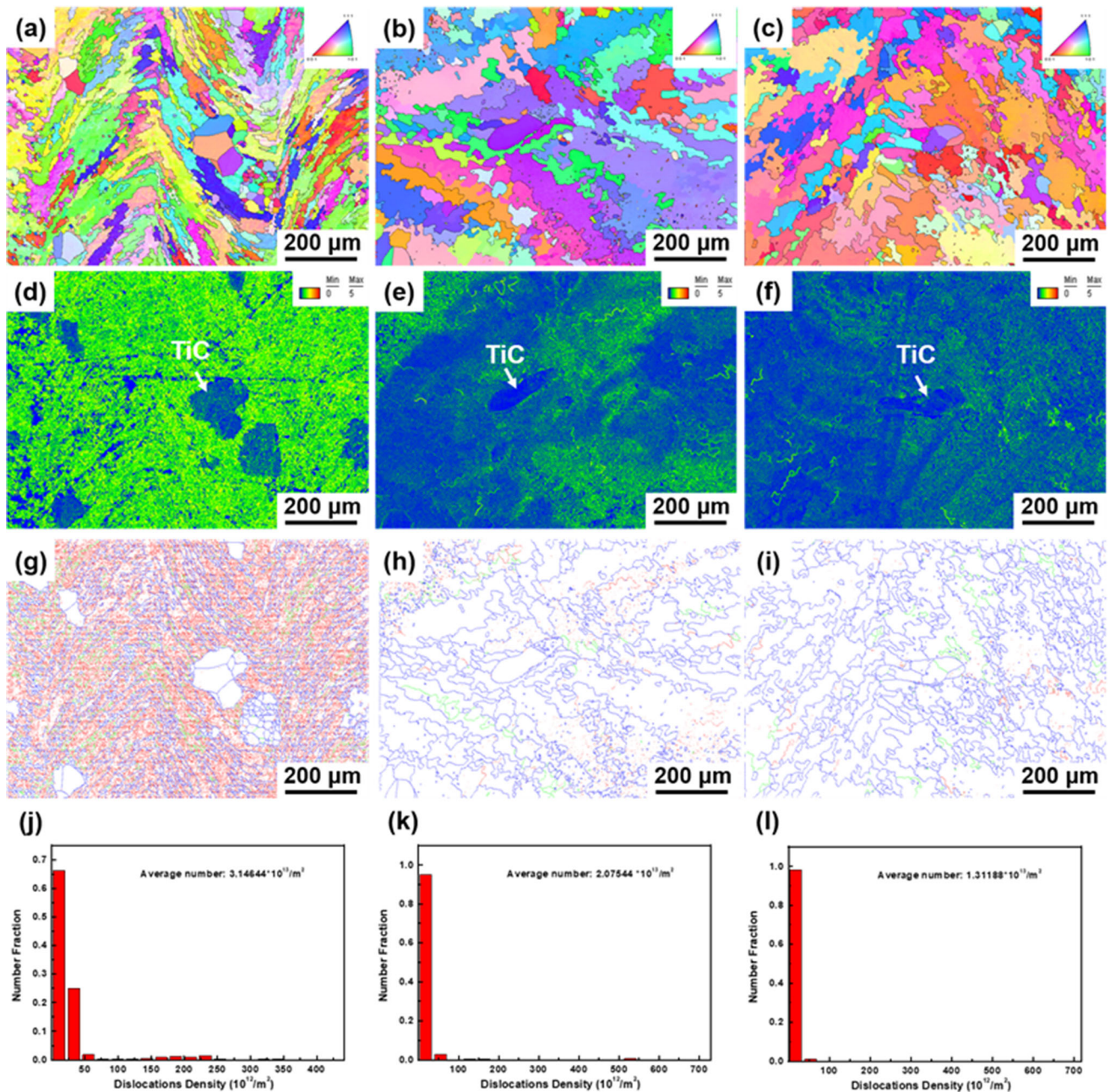
Fig. 10 The electron backscatter diffraction (EBSD) image of NiTi-5% TiC and heat treatment by 600 °C-2 h, 800 °C-2 h, respectively: (a)-(c) inverse pole figure (IPF) maps; (d)-(f) KAM map;(g)-(i) grain boundaries orientation maps; (j)-(l) Dislocations Density figure

Table 3 The numerical values of residual stress

Sample	E, GPa	K, MPa/°	M°	Residual stress at center, MPa
330W	50.324	− 853.6	− 0.4203	359
330W-600 °C	48.560	− 826.7	− 0.305	251
330W-800 °C	26.871	− 455.8	− 0.127	58

4. Conclusion

This article investigates the microstructure and mechanical properties of NiTi and NiTi with 5 wt.% TiC addition prepared by LENS. The residual stress, microstructure, and mechanical properties of NiTi with 5 wt.% TiC addition are controlled by heat treatment. The main conclusions are as follows:
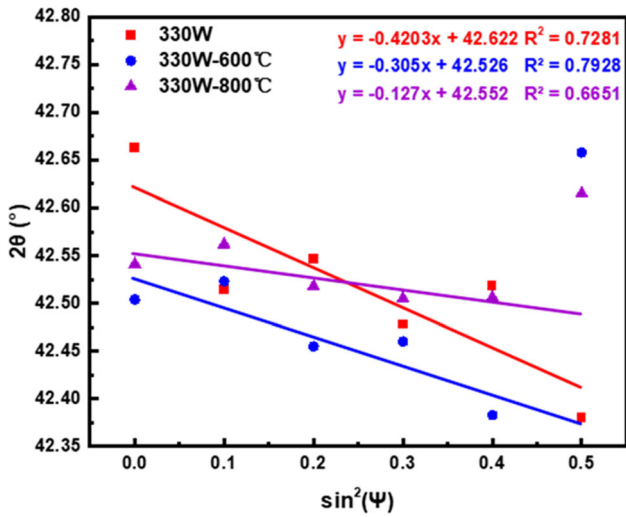
Fig. 11 The relationship between 2θ and sin²Ψ

1. The yield strength of NiTi SMAs with 5 wt.% TiC at 330W laser power is 531 MPa, which is 47.1% higher than that of pure NiTi SMAs (361 MPa). The elongations are 8.36 and 1.5%, respectively.
2. There are three distinct types of TiC with different morphologies inside NiTi with 5 wt.% TiC: GPT, DPT, and UMT. The generation of DPT led to the change of the local Ni/Ti ratio in the NiTi matrix, which widen the phase transition temperature.
3. The dislocation density of NiTi with 5 wt.% TiC is effectively reduced by changing the heat treatment temperature, showing a reduction of 58.31%. Compared with as-built NiTi-5% TiC, the residual stress of the sample after heat treatment at 800°C is reduced by about 80%
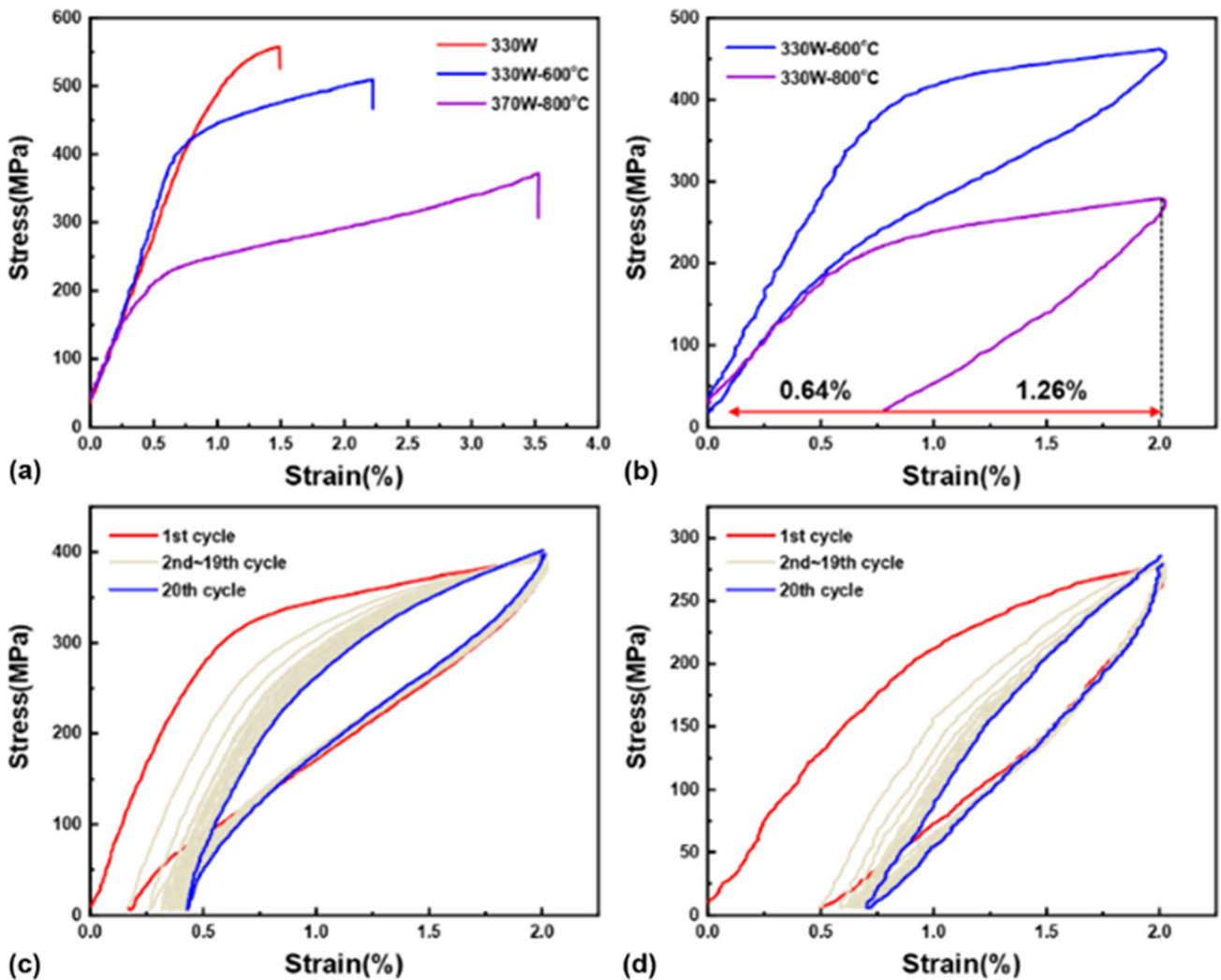

Fig. 12 (a) Strain-stress curves of NiTi-5% TiC by heat treatment; (b) Superelasticity and shape memory effect of NiTi-5% TiC by heat treatment; Cyclic stability of NiTi-5% TiC: (c) heat treatment by 600 °C-2 h; (d) heat treatment by 800 °C-2 h

References

1. K. Otsuka and X. Ren, Recent Developments in the Research of Shape Memory Alloys, *Intermetallics*, 1999, **7**, p 511–528.
2. D.C. Lagoudas, Shape Memory Alloys: Modeling and Engineering Applications, *Springer Science & Business Media*, 2008
3. D.J. Hartl and D.C. Lagoudas, Aerospace Applications of Shape Memory Alloys, *Proc. Ins.t Mech. Eng. G J. Aerosp. Eng.*, 2007, **221**, p 535–552.
4. J.M. Jani, M. Leary, A. Subic, and M.A. Gibson, A Review of Shape Memory Alloy Research, Applications and Opportunities, *Mater. Des.*, 2014, **56**, p 1078–1113.
5. H. Hou, E. Simsek, T. Ma, N.S. Johnson, S. Qian, C. Cissé, D. Stasak, N. Al Hasan, L. Zhou, and Y. Hwang, Fatigue-Resistant High-Performance Elastocaloric Materials Made by Additive Manufacturing, *Science*, 2019, **366**, p 1116–1121.
6. H. Hou, E. Simsek, D. Stasak, N. Al Hasan, S. Qian, R. Ott, J. Cui, and I. Takeuchi, Elastocaloric Cooling of Additive Manufactured Shape Memory Alloys with Large Latent Heat, *J. Phys. D*, 2017, **50**, p 404001.
7. B. Li, L. Wang, B. Wang, D. Li, and J.P. Oliveira, Electron Beam Freeform Fabrication of NiTi Shape Memory Alloys: Crystallography, Martensitic Transformation, and Functional Response, *Mater. Sci. Eng. A*, 2020, **843**, p 143135.
8. F.B. Teshome, B. Peng, J.P. Oliveira, J. Shen, S. Ao, H. Li, L. Chen, C. Tan, X. Song, N. Zhou, and Z. Zeng, Role of Pd interlayer on NiTi to Ti6Al4V Laser Welded Joints: Microstructural Evolution and Strengthening Mechanisms, *Mater. Des.*, 2023, **228**, 111845
9. J.P. Oliveira, D. Barbosa, F.B. Fernandes, and R.M. Miranda, Tungsten Inert Gas (TIG) Welding of Ni-rich NiTi Plates: Functional Behavior, *Smart Mater. Struct.*, 2016, **25**(3), p 03LT01.
10. P. Li, Y. Gong, C. Liang, Y. Yang, and M. Cai, Effect of Post-Heat Treatment on Residual Stress and Tensile Strength of Hybrid Additive and Subtractive Manufacturing, *Int. J. Adv. Manuf.*, 2019, **103**, p 2579–2592.
11. D. Mari and D. Dunand, NiTi and NiTi-TiC Composites: Part 1 Transformation and Thermal Cycling Behavior, *Metall Mater Trans A Phys Metall Mater*, 1995, **26**, p 2833–2847.
12. K. Fukami-Ushiro and D. Dunand, NiTi, and NiTi-TiC composites: Part III Shape-Memory Recovery, *Metall Mater Trans A Phys Metall Mater*, 1996, **27**, p 193–203.
13. D. Zhang, Y. Li, H. Wang, and W. Cong, An Investigation on Ni_4Ti_3 Phase Precipitation and its Effects in Laser Directed Energy Deposition of TiC-NiTi Composites, *Mater. Sci. Eng. A*, 2021, **809**, 140976
14. C Emmelmann, J Kranz, D Herzog, and E Wycisk, (2013) Laser Additive Manufacturing of Metals, *Laser Technology in Biomimetics: Basics and Applications*, , 143-162
15. D. Herzog, V. Seyda, E. Wycisk, and C. Emmelmann, Additive Manufacturing of Metals, *Acta Mater.*, 2016, **117**, p 371–392.
16. C. Li, Z. Liu, X. Fang, and Y. Guo, Residual Stress in Metal Additive Manufacturing, *Procedia Cirp*, 2018, **71**, p 348–353.
17. E. Capello, Residual Stresses in Turning: Part I: Influence of Process Parameters, *J. Mater. Process. Technol.*, 2005, **160**(2), p 221–228.
18. E.M. Anawa and A.G. Olabi, Control of Welding Residual Stress for Dissimilar Laser Welded Materials, *J. Mater. Process. Technol.*, 2008, **204**(1–3), p 22–33.
19. J.E. Choi, J.N. Waddell, and M.V. Swain, Pressed Ceramics onto Zirconia. Part 2: Indentation Fracture and Influence of Cooling Rate on Residual Stresses, *Dent. Mater.*, 2011, **27**(11), p 1111–1118.
20. S.G. Chen, H.J. Gao, Q. Wu, Z.H. Gao, and X. Zhou, Review on Residual Stresses in Metal Additive Manufacturing: Formation Mechanisms, Parameter Dependencies, Prediction and Control Approaches, *J. Mater. Res. Technol.*, 2022, **17**, p 2950–2974.
21. J. Robinson, I. Ashton, P. Fox, E. Jones, and C. Sutcliffe, Determination of the Effect of Scan Strategy on Residual Stress in Laser Powder Bed Fusion Additive Manufacturing, *Addit. Manuf.*, 2018, **23**, p 13–24.
22. Y. Zhang, H. Jing, L. Xu, Y. Han, and L. Zhao, Effects of Different Scanning Patterns on Nickel Alloy-Directed Energy Deposition Based on Thermal Analysis, *Virtual Phys Prototyp.*, 2021, **16**, p 98-S115.
23. L. Mugwagwa, D. Dimitrov, S. Matope, and I. Yadroitsev, Influence of Process Parameters on Residual Stress Related Distortions in Selective Laser Melting, *Procedia Manuf.*, 2018, **21**, p 92–99.
24. T. Simson, A. Emmel, A. Dwars, and J. Böhm, Residual Stress Measurements on AISI 316L Samples Manufactured by Selective Laser Melting, *Addit. Manuf.*, 2017, **17**, p 183–189.
25. M. Shiomi, K. Osakada, K. Nakamura, T. Yamashita, and F. Abe, Residual Stress Within Metallic Model Made by Selective Laser Melting Process, *CIRP Ann. Manuf. Technol.*, 2004, **53**, p 195–198.
26. D. Buchbinder, W. Meiners, N. Pirch, K. Wissenbach, and J. Schrage, Investigation on Reducing Distortion by Preheating during Manufacture of Aluminum Components using Selective Laser Melting, *J. Laser Appl.*, 2014, **26**, 012004
27. Z. Tong, X. Ren, J. Jiao, W. Zhou, Y. Ren, Y. Ye, E.A. Larson, and J. Gu, Laser Additive Manufacturing of FeCrCoMnNi High-Entropy Alloy: Effect of Heat Treatment on Microstructure, Residual Stress and Mechanical Property, *J. Alloys Compd.*, 2019, **785**, p 1144–1159.
28. Y. Zhan, H. Xu, W. Du, and C. Liu, Research on the Influence of Heat Treatment on Residual Stress of TC4 Alloy Produced by Laser Additive Manufacturing Based on laser ultrasonic technique, *Ultrasonics*, 2021, **115**, 106466
29. J. Frenzel, Z. Zhang, C. Somsen, K. Neuking, and G. Eggeler, Influence of Carbon on Martensitic Phase Transformations in NiTi Shape Memory Alloys, *Acta Mater.*, 2007, **55**, p 1331–1341.
30. G. Ma, C. Yu, B. Tang, Y. Li, F. Niu, D. Wu, G. Bi, and S. Liu, High-mass-Proportion TiCp/Ti6Al4V Titanium Matrix Composites Prepared by Directed Energy Deposition, *Addit. Manuf.*, 2020, **35**, 101323
31. G. Ma, X. Liu, C. Song, F. Niu, and D. Wu, TiCp Reinforced Ti6Al4V of Follow-up Synchronous Electromagnetic Induction-Laser Hybrid Directed Energy Deposition: Microstructure Evolution and Mechanical Properties, *Addit. Manuf.*, 2022, **59**, 103087
32. J. dos Da Silva, T. Santos, and A. Strohaecker, Reguly, Study of Structure/Property Relationships of Diffusion Bonded Ti6Al4V+ 10 wt-% TiC Particulate Composite, *Sci. Technol. Weld. Join.*, 2005, **10**, p 413–417.
33. L. Yu, K. Chen, Y. Zhang, J. Liu, L. Yang, and Y. Shi, Microstructures and Mechanical Properties of NiTi Shape Memory Alloys Fabricated by Wire Arc Additive Manufacturing, *J. Alloys Compd.*, 2022, **892**, 162193
34. R. Vaidyanathan, M. Bourke, and D. Dunand, Stress-induced Martensitic Transformations in NiTi and NiTi-TiC Composites Investigated by Neutron Diffraction, *Mater. Sci. Eng. A*, 1999, **273**, p 404–409.
35. U.S. Bertoli, G. Guss, S. Wu, M.J. Matthews, and J.M. Schoenung, In-situ Characterization of Laser-powder Interaction and Cooling Rates through High-speed Imaging of Powder Bed Fusion Additive Manufacturing, *Mater. Des.*, 2017, **135**, p 385–396.
36. C. Ma, D. Gu, D. Dai, G. Yu, M. Xia, and H. Chen, Thermodynamic Behaviour and Formation Mechanism of Novel Titanium Carbide Dendritic Crystals Within a molten Pool of Selective Laser Melting TiC/Ti-Ni Composites, *CrystEngComm*, 2017, **19**, p 1089–1099.
37. R. Vaidyanathan, D. Dunand, and U. Ramamurty, Fatigue Crack-growth in Shape-Memory NiTi and NiTi-TiC Composites, *Mater. Sci. Eng. A*, 2000, **289**, p 208–216.
38. L. Li, J. Wang, P. Lin, and H. Liu, Microstructure and Mechanical Properties of Functionally Graded TiCp/Ti6Al4V Composite Fabricated by Laser Melting Deposition, *Ceram. Int.*, 2017, **43**, p 16638–16651.
39. X. Meng, J. Min, Z. Sun, W. Zhang, H. Chang, and Y. Han, Columnar to Equiaxed Grain Transition of Laser Deposited Ti6Al4V using Nanosized B4C Particles, *Compos. B Eng.*, 2021, **212**, 108667

40. C. Hong, D. Gu, D. Dai, M. Alkhayat, W. Urban, P. Yuan, S. Cao, A. Gasser, A. Weisheit, and I. Kelbassa, Laser Additive Manufacturing of Ultrafine TiC Particle Reinforced Inconel 625 Based Composite Parts: Tailored Microstructures and Enhanced Performance, *Mater. Sci. Eng. A*, 2015, **635**, p 118–128.

41. S. Saedi, A.S. Turabi, M.T. Andani, C. Haberland, H. Karaca, and M. Elahinia, The Influence of Heat Treatment on the Thermomechanical Response of Ni-rich NiTi Alloys Manufactured by Selective Laser Melting, *J. Alloys Compd.*, 2016, **677**, p 204–210.

42. J. Khalil-Allafi, A. Dlouhy, and G. Eggeler, Ni4Ti3-Precipitation during Aging of NiTi Shape Memory Alloys and its Influence on Martensitic Phase Transformations, *Acta Mater.*, 2002, **50**, p 4255–4274.

43. J. Zhu, H.-H. Wu, Y. Wu, H. Wang, T. Zhang, H. Xiao, Y. Wang, and S.-Q. Shi, Influence of Ni4Ti3 Precipitation on Martensitic Transformations in NiTi Shape Memory Alloy: R phase Transformation, *Acta Mater.*, 2021, **207**, 116665

44. N. Zhou, C. Shen, M.-X. Wagner, G. Eggeler, M. Mills, and Y. Wang, Effect of Ni4Ti3 Precipitation on Martensitic Transformation in Ti-Ni, *Acta Mater.*, 2010, **58**, p 6685–6694.

45. K. Otsuka and X. Ren, Physical metallurgy of Ti-Ni-Based Shape Memory Alloys, *Prog. Mater. Sci.*, 2005, **50**, p 511–678.

46. A.F. Chadwick and P.W. Voorhees, The Development of Grain Structure during Additive Manufacturing, *Acta Mater.*, 2021, **211**, 116862

47. S. Gorsse, C. Hutchinson, M. Gouné, and R. Banerjee, Additive Manufacturing of Metals: A Brief Review of the Characteristic Microstructures and Properties of Steels, Ti-6Al-4V and high-entropy alloys, *Sci. Technol. Adv. Mater.*, 2017, **18**, p 584–610.

48. J. Pešička, R. Kužel, A. Dronhofer, and G. Eggeler, The Evolution of Dislocation Density during Heat Treatment and Creep of Tempered Martensite Ferritic Steels, *Acta Mater.*, 2003, **51**, p 4847–4862.

49. B.D. Cullity (1956), Elements of X-ray Diffraction, Addison-Wesley Publishing,

50. V. Sinha and V. Godaba, Residual Stress Measurement in Worked and Heat Treated Steel by X-ray Diffractometry, *Mater. Sci. Eng. A*, 2008, **488**, p 491–495.

51. C. Chang and Y. Koo, X-Ray Measurement of Lattice Strains in Textured Low Carbon Steel under Uniaxial Loading, *Metall Mater Trans A Phys Metall Mater*, 1995, **26**, p 629–632.

52. B. He, B. Hu, H. Yen, G. Cheng, Z. Wang, H. Luo, and M. Huang, High dislocation density–induced large ductility in deformed and partitioned steels, *Science*, 2017, **357**, p 1029–1032.

53. J. Frenzel, E.P. George, A. Dlouhy, C. Somsen, M.-X. Wagner, and G. Eggeler, Influence of Ni on Martensitic Phase Transformations in NiTi Shape Memory Alloys, *Acta Mater.*, 2010, **58**, p 3444–3458.

54. J.P. Oliveira, R.M. Miranda, N. Schell, and F.B. Fernandes, High Strain and Long Duration Cycling Behavior of Laser Welded NiTi Sheets, *Int. J. Fatigue*, 2016, **83**, p 195–200.

55. J.P. Oliveira, F.B. Fernandes, N. Schell, and R.M. Miranda, Martensite Stabilization during Superelastic Cycling of Laser Welded NiTi Plates, *Mater. Lett.*, 2016, **171**, p 273–276.